

Influence of ZnO concentration on the optical and photocatalytic properties of Ni-doped ZnS/ZnO nanocomposite

W W ANKU*, S O B OPPONG, S K SHUKLA and P P GOVENDER

Department of Applied Chemistry, University of Johannesburg, P.O. Box 17011, 2028 Johannesburg, South Africa

MS received 11 March 2016; accepted 15 April 2016

Abstract. Photocatalysts consisting of nickel-doped ZnS/ZnO core shell nanocomposites with varying concentrations of ZnO was synthesized through chemical precipitation method. The catalyst was deployed in photocatalytic degradation of indigo carmine dye as a model organic pollutant. Characterization of the samples was achieved through the use of X-ray powder diffraction, Fourier transform infrared spectroscopy, transmission electron microscopy, scanning electron microscopy, UV–vis spectroscopy and energy dispersive spectroscopy. The composites consist of wurtzite ZnO phase deposited on cubic ZnS. Optical absorption, crystallite sizes and photocatalytic degradation efficiency increased with increasing ZnO concentration. Bandgap values of ZnS also decreased appreciably with increase in ZnO concentration. Ni-doped ZnS/(0.5 M ZnO) was identified as the most efficient catalyst with 91% dye degradation efficiency at a rate of $15.38 \times 10^{-3} \text{ min}^{-1}$ in 180 min. Meanwhile, the pristine ZnS degraded 25% of the dye at the rate of $1.53 \times 10^{-3} \text{ min}^{-1}$ within the same time. The Ni-doped ZnS/(0.5 M ZnO) was used to degrade the dye on the basis of influence of factors such as solution temperature, hydrogen peroxide (H_2O_2) and ethanol contents. Dye degradation increased with increase in temperature, but decreased with ethanol content. H_2O_2 content initially caused enhanced dye degradation but the efficiency decreased with higher H_2O_2 content.

Keywords. Nanocomposite; ZnO; ZnS; metal doped; photocatalytic degradation; dyes.

1. Introduction

Semiconductor photocatalysis is currently regarded as an appropriate technology for mineralization of organic pollutants, particularly dyes from industrial wastewater. This technology has attracted much attention due to its low cost and environmentally friendly nature [1,2]. Several semiconductor inorganic solids such as TiO_2 , ZnO, ZrO_2 and ZnS have been studied for their photocatalytic activities for the removal of organic pollutants from wastewater [3,4].

Nanocrystals of elements from groups II–VI are among the most studied semiconductor compounds for their photocatalytic activities, as they possess size-tunable and exciting optical properties owing to their strong quantum confinement effect [5]. Among this group of compounds is zinc sulphide (ZnS) nanoparticle, which has a wide bandgap value of 3.67 eV at room temperature and has been tried in photocatalytic degradation studies [6]. However, due to its wide bandgap, ZnS lacks the ability to absorb visible light, which is required for its effective photocatalytic activity, but rather absorbs ultraviolet (UV) light in the wavelength range of 385 nm. This phenomenon significantly restricts its practical application in heterogeneous photocatalysis [7]. In addition, ZnS nanoparticle also suffers from the rapid recombination of the photogenerated electrons and holes, which further

hamper its efficiency as a photocatalyst. To enhance its efficiency as a photocatalyst, ZnS nanoparticle needs to be modified so as to make it visible light active and minimize the electron–hole recombination rates [8,9].

As far as the enhancement of photocatalytic activity of a semiconductor photocatalyst is concerned, coupling of two metal oxide semiconductors resulting in a core/shell nanocomposite has been studied. These core/shell composites are known to effectively improve the visible light activity and reduce the electron–hole recombination rate of the photocatalyst under consideration [10,11]. Research has proved that coupling ZnS with ZnO will result in an effective photocatalyst as the ZnS/ZnO heterostructure could lessen the charge carrier recombination rate with improved visible light activity [12,13]. Nonetheless, earlier research activities focused mostly on ZnS/ZnO nanocomposites only. Information on transition metal-modified ZnS/ZnO for improved photocatalytic activity is limited.

Transition metal ions are purposely used to modify semiconductor nanoparticles to enhance their photocatalytic activity in the visible light region [14] and to serve as recombination centres in order to improve charge separation. Nickel ion (Ni^{2+}) can be an effective dopant to modify ZnS, as the ionic radius of Ni^{2+} (0.68 Å) is close to that of Zn^{2+} (0.74 Å) [15]. This means that Ni^{2+} can easily substitute Zn^{2+} in a crystal lattice and create an impurity energy level leading to superior visible light response of ZnS.

With ZnS being a non-toxic semiconductor material with catalytic properties coupled with the abundant information

* Author for correspondence (williamanku85@gmail.com)

available in relation to the efficient photocatalytic properties of ZnO, a Ni-ZnS/ZnO core/shell nanocomposite is envisaged to be a promising photocatalyst. The objective of this study was to synthesize an effective photocatalyst consisting of Ni-doped ZnS/ZnO nanocomposite through chemical precipitation method. The ZnO concentration was varied for a fixed amount of ZnS nanoparticles in order to assess the effect of ZnO thickness on the photocatalytic activity of the Ni-doped ZnS/ZnO nanocomposite. The Ni-doped ZnS/ZnO photocatalyst was deployed in the degradation of indigo carmine dye, used as a representative organic pollutant under simulated visible light. The influence of factors such as solution temperature, hydrogen peroxide and ethanol content on the photocatalytic degradation efficiency of the dye was also considered.

2. Experimental

2.1 Materials

All the chemicals used in this experiment including sodium sulphide (Na_2S), zinc acetate dihydrate ($\text{Zn}(\text{CH}_3\text{COO})_2 \cdot 2\text{H}_2\text{O}$), absolute ethanol ($\text{CH}_3\text{CH}_2\text{OH}$), nickel nitrate hexahydrate $\text{Ni}(\text{NO}_3)_2 \cdot 6\text{H}_2\text{O}$, indigo carmine and sodium hydroxide (NaOH) were all procured from Sigma-Aldrich. Deionized (DI) water was used throughout the experiment. The standard indigo carmine solution (1000 ppm) was prepared by dissolving the appropriate amount in 1 litre DI water. The standard solution was then diluted to obtain the desired 20 ppm solution.

2.2 Synthesis of Ni-ZnS/ZnO nanocomposite

The Ni-doped ZnS/ZnO synthesis was a two-step process. The Ni-ZnS nanoparticle was first synthesized followed by the deposition of ZnO on the Ni-ZnS. First, 50 ml solutions of 0.5 M Na_2S and $\text{Zn}(\text{CH}_3\text{COO})_2 \cdot 2\text{H}_2\text{O}$ were each prepared. Then, a calculated amount of $\text{Ni}(\text{NO}_3)_2 \cdot 6\text{H}_2\text{O}$ representing 0.6% Ni was dissolved in the $\text{Zn}(\text{CH}_3\text{COO})_2 \cdot 2\text{H}_2\text{O}$ solution with constant magnetic stirring for 1 h. The Na_2S solution was added drop-by-drop to the $\text{Zn}(\text{CH}_3\text{COO})_2 \cdot 2\text{H}_2\text{O}$ solution at room temperature. The Ni-ZnS precipitate was formed soon after addition of the Na_2S solution. The stirring was continued for another 30 min after which the precipitate was separated by centrifugation at 7500 rpm for 4 min, washed several times with DI water and ethanol and dried at 100°C for 12 h.

In the second process, 0.5 g of the synthesized Ni-ZnS was dispersed in three beakers containing 200 ml DI water through sonication for 1 h. A quantity of 50 ml $\text{Zn}(\text{CH}_3\text{COO})_2 \cdot 2\text{H}_2\text{O}$ solutions of varied concentrations (0.1, 0.3 and 0.5 M) were added separately to each of the Ni-ZnS mixtures in the three beakers in a dropwise manner. The resultant mixtures were allowed to stir for 1 h. Thereafter, 3 M NaOH solution was added to each mixture drop-by-drop with continuous stirring until a pH of 10, by which time the

Ni-ZnS/ZnO nanocomposites were formed. The precipitates were separated by centrifugation (7500 rpm, 4 min), washed several times with DI water and ethanol and dried at 100°C for 12 h. The samples were later calcined at 300°C for 3 h and pulverized to obtain the powdered nanocomposites. For the purpose of comparison, pure ZnS nanoparticle was also synthesized following the same procedure for Ni-ZnS synthesis, but without the addition of $\text{Ni}(\text{NO}_3)_2 \cdot 6\text{H}_2\text{O}$.

2.3 Characterization

The synthesized nanocomposites were characterized using X-ray diffraction (XRD) pattern recorded on Philips PANalytical X'pert PRO X-ray diffractometer operating at 40 kV using $\text{Cu-K}\alpha$ radiation at a wavelength of 0.15406 nm. The measurement was performed over a diffraction angle range of $2\theta = 20\text{--}80^\circ$. UV-visible absorption spectra and diffuse reflectance were recorded using a UV-Vis spectrophotometer (Shimadzu UV-2450). Barium sulphate was used as the reflectance standard. Fourier transformed infrared (FTIR) spectroscopy was performed on PerkinElmer spectrometer (Spectrum 100) in the wavelength range of 400 to 4000 cm^{-1} . The FTIR analysis was performed by using KBr pellet. The surface morphology of the samples was examined by scanning electron microscopy (SEM) using a TESCAN (Vega 3 XMU) system. The elemental composition of the sample was obtained using energy dispersed X-ray (EDX) attached to SEM.

2.4 Evaluation of photocatalytic activity

The photocatalytic degradation potential of the synthesized ZnS, Ni-ZnS and Ni-ZnS/ZnO with 0.1, 0.3 and 0.5 M of ZnO were probed by applying them in the degradation of 20 mg l^{-1} solutions of indigo carmine dye under simulated visible light. In this process, 0.2 g of each photocatalyst was dispersed in 200 ml of 20 mg l^{-1} aqueous solution of indigo carmine dye. The mixtures were initially kept under continuous magnetic stirring without light illumination for 30 min to establish adsorption equilibrium between the catalyst and the dye solution. The mixtures were then illuminated at room temperature using a Port 9600 full-spectrum solar simulator equipped with 150 W ozone-free xenon lamp, and fit with a dichroic UV filter ($\lambda = 420\text{ nm}$). A volume of 5 ml of the illuminated solutions were withdrawn using disposable syringes fit with $0.45\text{ }\mu\text{m}$ PVDF membranes at 30 min intervals. The dye concentration in each withdrawn solution after illumination was determined using Shimadzu UV-2450 spectrophotometer at a wavelength of 610 nm. The experiments were carried out for 180 min at a stirring speed of 500 rpm at the solution pH. Discolouration efficiencies and kinetic studies were used to examine the photodegradation ability of the catalysts.

2.5 Effect of solution temperature on photodegradation

A 20 mg l^{-1} indigo carmine dye solution of 200 ml was degraded with 0.2 g catalyst under simulated visible light

illumination at different temperatures of 10, 25, 40, 50 and 60°C. The temperature was varied using a Lasec hotplate stirrer. The experiment was carried out for 180 min at a stirring speed of 500 rpm at the solution pH. Five ml aliquots of the illuminated solutions were taken after every 180 min and dye content remaining in the solution was determined.

2.6 Effect of H₂O₂ solution on photodegradation

Indigo carmine dye solution (200 ml, 20 mg l⁻¹) containing 0.2 g of the Ni-ZnS/ZnO catalyst and different volumes of 50% H₂O₂ solution (0, 0.5, 1.0, 1.5, 2 and 2.5 ml) were irradiated with simulated visible light. The experiment followed the same procedure as indicated above.

2.7 Effect of ethanol on photodegradation

In this experiment, the dye contents in the 5 ml aliquots of the illuminated dye solutions containing no ethanol, 1, 2 and 3 ml ethanol were determined by following the same degradation procedure as indicated above.

3. Results and discussion

3.1 XRD analysis

The XRD patterns of pure ZnS, Ni-ZnS and Ni-ZnS/ZnO composites with different ZnO concentrations are shown in figure 1. The XRD pattern of ZnS and Ni-ZnS (a and b in figure 1) displayed three peaks at 2θ values of 29°, 48.2° and 54.4° corresponding to (111), (220) and (311), respectively. These diffraction peaks can be indexed to cubic ZnS and corresponds well with JCPDS (file no. 5-0566) [16]. No peak corresponding to Ni oxide was found in the XRD pattern of Ni-ZnS/ZnO composite, indicating that the Ni²⁺ ion perfectly substituted the Zn²⁺ ion in the ZnS lattice structure, except for slight shift in peak positions to lower 2 theta values of the Ni-ZnS nanoparticle. In addition to the peaks observed for ZnS, new peaks are identified for ZnO in the XRD pattern of Ni-ZnS/ZnO nanocomposites with varying concentrations of ZnO (c–e in figure 1). These peaks which occurred at 31.6°, 34.3°, 36.2°, 62.7°, 67.9° and 69.0° correspond to diffraction planes of (100), (002), (101), (103), (112) and (201), respectively, indicating wurtzite crystalline structure of ZnO, according to standard JCPDS card number 80-0074. This observation confirmed the formation of ZnO on the surface of ZnS nanoparticles. It is observed, according to c–e in figure 1, that an increase in ZnO shell thickness produced corresponding increase in the peak intensities. The strong nature of the diffraction peaks is an indication of the high crystalline nature of the composites. Again, the full-width at half-maximum (FWHM) of the ZnS and Ni-ZnS peaks are broader than those of Ni-ZnS/ZnO. This indicates that the ZnS and Ni-ZnS have smaller crystallite sizes than the Ni-ZnS/ZnO composites.

The crystallite sizes of the catalysts were calculated according to Debye-Scherrer equation (Equation 1) [17] and

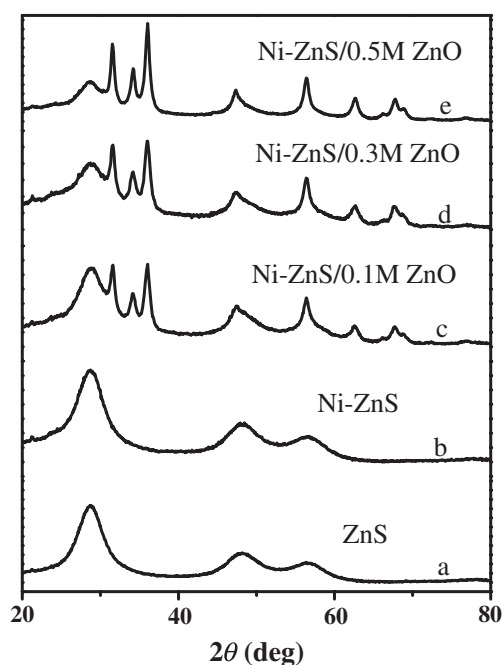


Figure 1. XRD patterns of ZnS, Ni-doped ZnS and Ni-doped ZnS/ZnO with varying concentrations of ZnO.

the particle sizes were found to be in the following order: 4.10 nm (ZnS) < 5.28 nm (Ni-ZnS) < 12.41 nm (Ni-ZnS/0.1 M ZnO) < 17.46 nm (Ni-ZnS/0.3 M ZnO) < 21.53 nm (Ni-ZnS/0.5 M ZnO). Thus, the crystallite size of the nanocomposites is proportional to the increase in ZnO concentration. The result of this analysis is presented in table 1. In Equation 1, D is the crystallite size, K a shape factor with a value of 0.9, λ the wavelength of the X-ray (0.15406 nm), β the value of FWHM in the radiation of (101) plan in 2θ scale and θ the Bragg's diffraction angle at the maximum.

$$D = \frac{K\lambda}{\beta \cos \theta}. \quad (1)$$

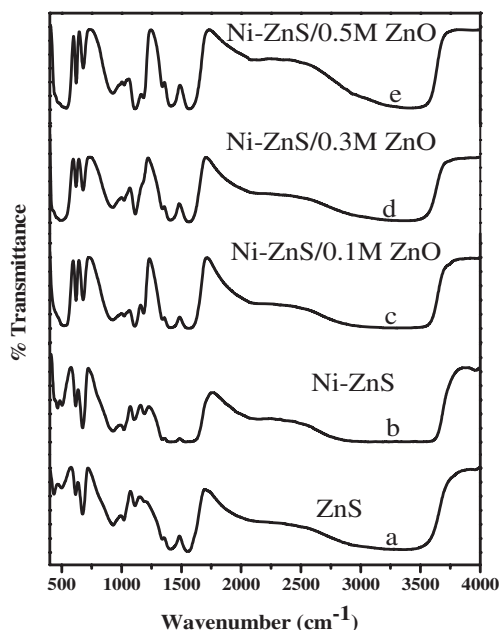
3.2 FTIR analysis

The FTIR spectra of the samples are presented in figure 2. In all the spectra, the broad absorption band around 3000–3600 cm⁻¹ is ascribed to hydrogen stretching frequency, i.e., –OH stretching due to water molecules on the surface of the nanoparticles. The weak band around 1600–2000 cm⁻¹ may be due to microstructure formation of the samples [18]. According to ZnS standard values, a band around 900–1500 cm⁻¹ is designated to oxygen stretching and bending frequency [18].

Characteristic peaks for inorganic ions are found around 1200–1100 cm⁻¹, while absorption peaks at 617 cm⁻¹ and below 500 cm⁻¹ are attributed to Zn-S stretching and metal-oxygen bonds [19]. In addition, based on the standard values of ZnO, bands at around 600 cm⁻¹ and below 500 cm⁻¹ can be accredited to Zn-O stretching and Zn-O-metal stretching modes [20]. The results of this analysis with respect to

Table 1. Crystallite size, bandgap, percent degradation based on catalyst doping and rate of indigo carmine degradation by ZnS, Ni-doped ZnS and Ni-doped ZnS/ZnO with varying concentration of ZnO.

Sample	Crystallite size (nm)	Bandgap (eV)	Degradation (%)	Rate (min^{-1})
ZnS	4.10	3.07	24.9	1.53×10^{-3}
Ni-ZnS	5.28	3.01	50.3	3.88×10^{-3}
Ni-ZnS/(0.3% ZnO)	12.41	2.91	77.7	8.60×10^{-3}
Ni-ZnS/(0.3% ZnO)	17.46	2.88	86.8	12.04×10^{-3}
Ni-ZnS/(0.3% ZnO)	21.53	2.76	91.4	15.38×10^{-3}

**Figure 2.** FTIR spectra of ZnS, Ni-doped ZnS and Ni-doped ZnS/ZnO with varying concentrations of ZnO.

ZnS, Ni-ZnS and ZnS/ZnO (0.1–0.3 M ZnO) spectra corroborate the above standard values with the exception of slight changes in peak intensities and broadness due to the ZnS/ZnO composite formation, and overlap of certain peaks. There are slight variations in peak intensities of ZnS and Ni-ZnS spectra (a and b in figure 2) due to Ni doping. It is observed, by comparing the spectra of Ni-ZnS/ZnO composites (with varying ZnO concentrations; c–e in figure 2) to that of ZnS (a in figure 2), that peaks below 600 cm^{-1} exhibited increased intensity and broadness probably due to the overlap of metal–oxygen (ZnS and ZnO) bands. Intensities of other peaks were also observed to increase with an increase in ZnO concentration. These observations confirm the successful synthesis of the Ni-doped ZnS/ZnO nanocomposites.

3.3 Morphology studies

The surface morphology, microstructure and elemental composition of the samples were studied using SEM, transmission electron microscopy (TEM) and EDX images. Figure 3a represents the SEM image of Ni-ZnS/0.5 M ZnO nanocomposite. The nanocomposites are small and almost spherical

in shape, with well-defined boundaries. The TEM image of Ni-ZnS/0.5 M ZnO (figure 3b) revealed that the Ni-ZnS/ZnO consist of both spherical and rod-like structures. The EDX spectrum of Ni-ZnS/ZnO, which is presented in figure 3c, revealed Zn, Ni, S, O as the components of the composite. The presence of these elements further proves the successful synthesis of Ni-ZnS/ZnO nanocomposites.

3.4 Optical studies

The UV–vis absorption spectra of the synthesized samples are presented in figure 4. The absorption edge of ZnS shifted to visible light region with Ni-doping and further increased with increase in ZnO concentration. Again, compared to pristine ZnS, the light absorption ability of all the samples in the entire visible light region red shifted with increased ZnO concentration. Thus, modification of ZnS with Ni and ZnO enhanced its visible light activity. The improved visible light absorption of the modified samples may be as a consequence of surface defect centre formation, mainly associated with the creation of oxygen vacancies due to the introduction of Ni ion [21,22]. It may also be ascribed to electronic interaction between ZnS and ZnO with an increase in ZnO concentration on ZnS [23], as this may lead to a rougher surface which reduces the reflection of incident light and increases the volume of optically active components [24]. The improved visible light absorption abilities of the Ni-ZnS and Ni-ZnS/ZnO composites compared to the bare ZnS is an indication that these catalysts may exhibit better photocatalytic activities than ZnS.

The bandgap values of the samples were calculated through the use of Kubelka-Munk equation (Equation 2) [25], derived from the UV–vis diffuse reflectance data of this analysis.

$$F(R) = \frac{(1 - R)}{2R}, \quad (2)$$

where the reflectance (R) = $R_{\text{sample}}/R_{\text{reference}}$.

The Kubelka-Munk function permits the construction of a Tauc plot ($[(F(R) * h\nu)^n \text{ vs. photo energy } (h\nu)]$), where the value of n depends on the type of semiconductor material under consideration. The value of $n = 1/2$ for a direct allowed bandgap semiconductor, $n = 2$ for an indirect bandgap semiconductor material and $n = 3$ for direct forbidden semiconductor material [26]. The Tauc plot obtained in this analysis is depicted in figure 5. The bandgap values of

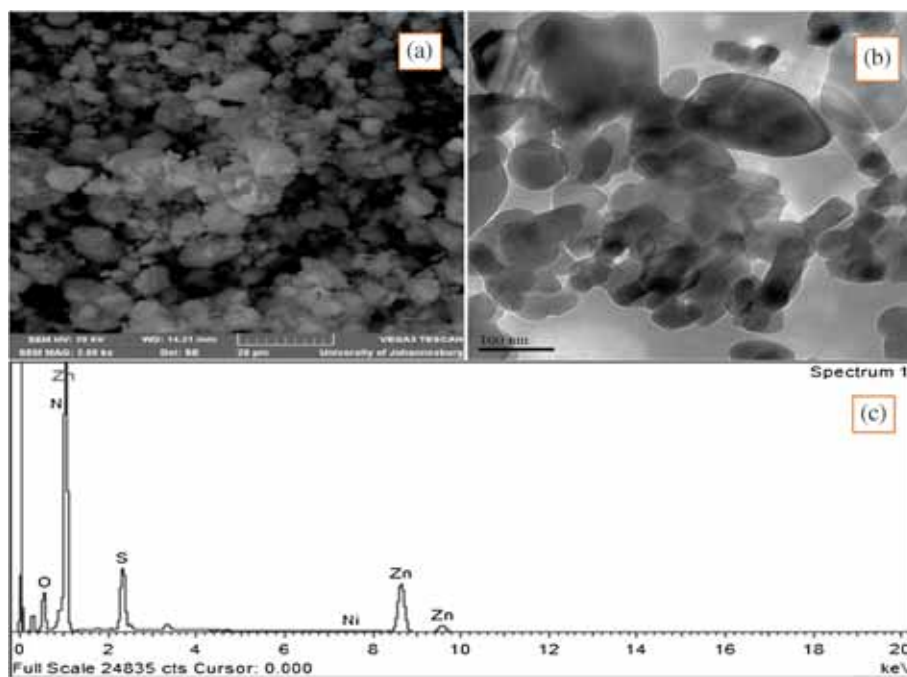


Figure 3. (a) SEM image of Ni-doped ZnS/0.5 M ZnO, (b) TEM image of Ni-doped ZnS/0.5 M ZnO and (c) EDX spectrum of Ni-doped ZnS/0.5 M ZnO.

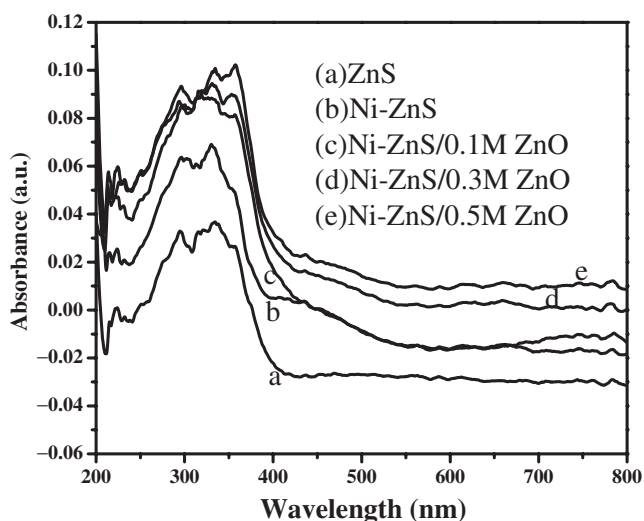


Figure 4. UV-visible spectra of ZnS, Ni-doped ZnS and Ni-doped ZnS/ZnO with varying concentrations of ZnO.

the samples were obtained by the extrapolation of Kubelka-Munk function to $F(R) = 0$ and the values are presented in table 1. The values were observed to decrease in the following order: ZnS (3.07 eV) > Ni-ZnS (3.01 eV) > Ni-ZnS/(0.1 M ZnO) (2.91 eV) > Ni-ZnS/(0.3 M ZnO) (2.88 eV) > Ni-ZnS/(0.5 M ZnO) (2.76 eV). Thus, the bandgap of ZnS decreased when doped with Ni and further decreased with increase in ZnO concentration. As the material size becomes larger, the bandgap decreases resulting in a change in its optical and electrical properties rendering it appropriate for other applications [27], such as photocatalysis. The modified

samples with reduced bandgap are therefore expected to have higher photocatalytic activities than the bare ZnS. The inverse relationship observed between the bandgap values and the nanoparticles size may be attributed to the quantum confinement effect [28].

3.5 Photocatalytic degradation studies

Photocatalytic degradation studies of the synthesized catalysts was achieved through the degradation of 20 mg l⁻¹ (200 ml) indigo carmine dye aqueous solution with 0.2 g of the catalysts in 180 min under simulated visible light. The degradation experiment was based on the influence of parameters, such as catalyst doping, effects of solution temperature, hydrogen peroxide (H₂O₂) and alcohol. The experiment was initially based on the effect of catalyst doping from which the best photocatalyst was identified. The effects of solution temperature, hydrogen peroxide and alcohol on the degradation efficiency of the best photocatalyst was then assessed.

3.5a Effect of catalyst doping: The indigo carmine dye photocatalytic degradation efficiency profile for ZnS, Ni-ZnS, Ni-ZnS/(0.1 M ZnO), Ni-ZnS/(0.3 M ZnO) and Ni-ZnS/(0.5 M ZnO) is shown in figure 6 and the corresponding data are presented in table 1. The results show that all the modified catalyst demonstrated better photocatalytic degradation efficiency than the pristine ZnS. It can therefore be stated that modification of ZnS with Ni and ZnO produced effective photocatalysts for the degradation of indigo carmine dye. Doping of Ni²⁺ ion onto ZnS was observed to improve its photodegradation efficiency and the efficiency

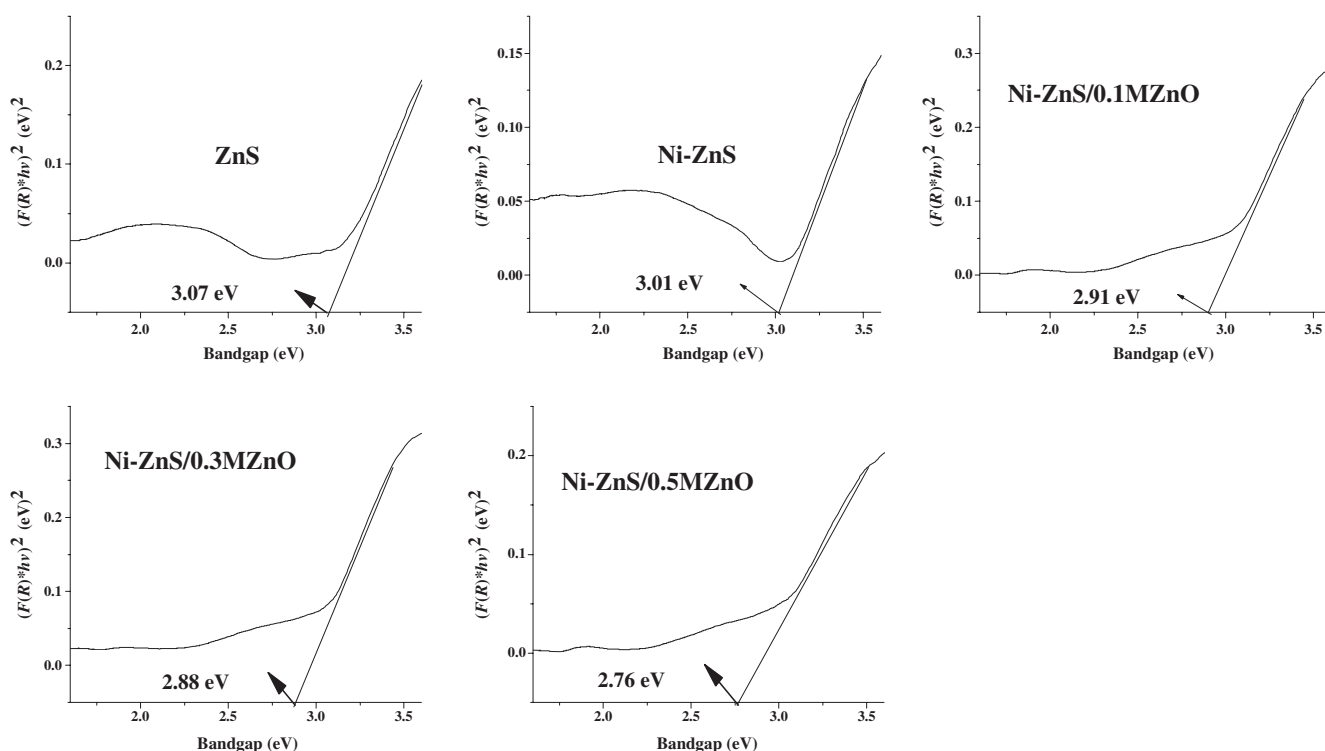


Figure 5. Tauc plots for ZnS, Ni-doped ZnS and Ni-doped ZnS/ZnO with varying concentrations of ZnO.

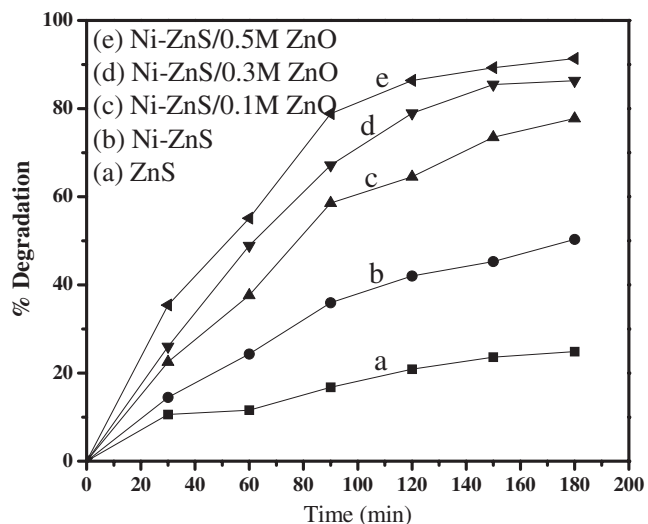


Figure 6. Indigo carmine degradation profile of ZnS, Ni-doped ZnS and Ni-doped ZnS/ZnO with varying concentrations of ZnO at room temperature and solution pH.

was augmented with ZnO. A direct relationship between ZnO concentration and photocatalytic degradation efficiency was observed with Ni-ZnS/(0.5 M ZnO) making it the best photocatalyst. The degradation efficiencies of the catalysts were thus identified to be in the order: ZnS < Ni-ZnS < Ni-ZnS/(0.1 M ZnO) < Ni-ZnS/(0.3 M ZnO) < Ni-ZnS/(0.5 M ZnO).

The pseudo-first-order kinetic model (Equation 3) was applied to the experimental data, through which the rate

constants (K_a) of degradation of the dye were determined from the slopes of the plot of $\ln(C_0/C)$ against time. The plots are displayed in figure 7 and the rate constants values are provided in table 1.

$$\ln \frac{C_0}{C} = K_a t \quad (3)$$

In Equation 3, C_0/C is the normalized concentration of the dye, t the reaction time and K_a the apparent rate constant of the reaction. According to figure 7, ZnS, the least efficient photocatalyst, degraded the dye at a rate of $1.53 \times 10^{-3} \text{ min}^{-1}$ while the most efficient catalyst (Ni-ZnS/(0.5 M ZnO) had a degradation rate of $15.38 \times 10^{-3} \text{ min}^{-1}$. Thus, Ni-ZnS/(0.5 M ZnO) degraded the dye about 10 times faster than ZnS, a further confirmation of Ni-ZnS/(0.5 M ZnO) being the most efficient catalyst. The improved photocatalytic activities of Ni-ZnS and Ni-ZnS/(0.1–0.5 M ZnO) over that of ZnS can be attributed to their high visible light activities and reduced bandgap values.

The best photocatalyst, Ni-ZnS/(0.5 M ZnO), was then used to study the effect of solution temperature, H_2O_2 and ethanol contents of the dye degradation efficiency.

3.5b Effect of solution temperature: Figure 8 shows the percentage degradation efficiency of the dye at different dye solution temperatures. It is obvious, according to figure 8, that temperature has a noticeable effect on the degradation efficiency of the dye. Degradation efficiency increased with increase in temperature from 10, 25, 40, 50 and 60°C. The degradation efficiency increased from 91.4% at the solution

temperature to 95.8% at 60°C. This result can be explained on the basis that an increase in temperature increased the rate of dispersion of the dye molecules on the surface and the internal pores of the catalyst resulting in enhanced degradation. The linear relationship between percent degradation and increased temperature indicates that the process is endothermic in nature.

3.5c Effect of H_2O_2 content: As electron-hole recombination is one of the hindrances for efficient deployment of the photocatalytic degradation process, addition of electron acceptors such as H_2O_2 are expected to lessen the electron-hole recombination, thereby enhancing the degradation process. With increase in H_2O_2 content from 0 to

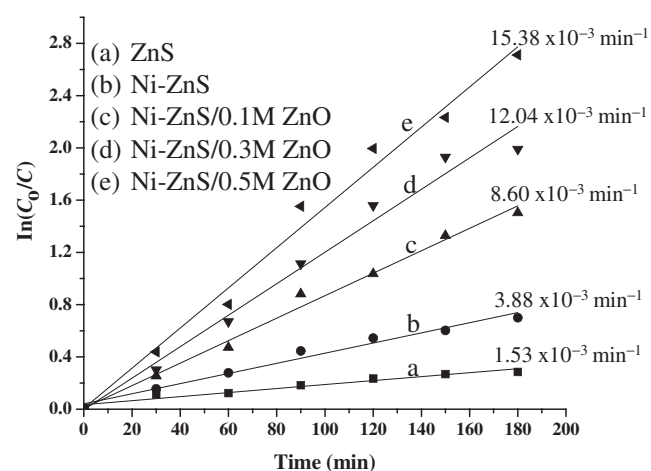


Figure 7. Kinetics of indigo carmine degradation by ZnS, Ni-doped ZnS and Ni-doped ZnS/ZnO with varying concentrations of ZnO at room temperature and solution pH.

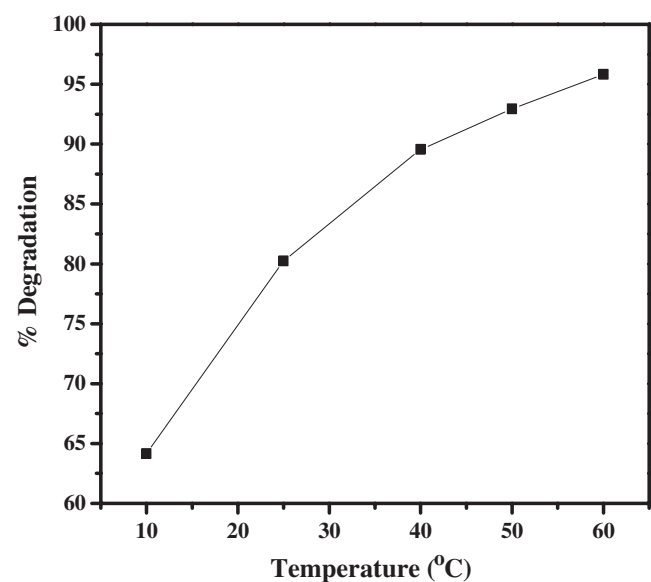


Figure 8. Effect of varying temperature on percent degradation of indigo carmine by Ni-doped ZnS/0.5 M ZnO at solution pH.

1.0 ml, the percentage degradation efficiency of the dye using (Ni-ZnS/(0.5 M ZnO) increased sharply from 91.4% at 0 ml to 96.5% at 1.0 ml. However, increase in the H_2O_2 content after 1 ml caused a steady decrease in the degradation efficiency of the dye up until 2.5 ml when the degradation efficiency reduced to 89.6% (figure 9). These occurrences can be explained as follows: At low concentration H_2O_2 increases the rate of degradation due to its ability to appropriately trap the electrons, thereby inhibiting the electron-hole pair recombination and thus increasing hydroxyl radical formation on the surface of the catalyst [29,30]. On the other hand, an increase in the electron acceptor concentration beyond a certain level causes it to react with the hydroxyl radical and scavenge for the photogenerated holes. In addition, H_2O_2 can modify the catalyst surface and probably decreased its photocatalytic activity [31].

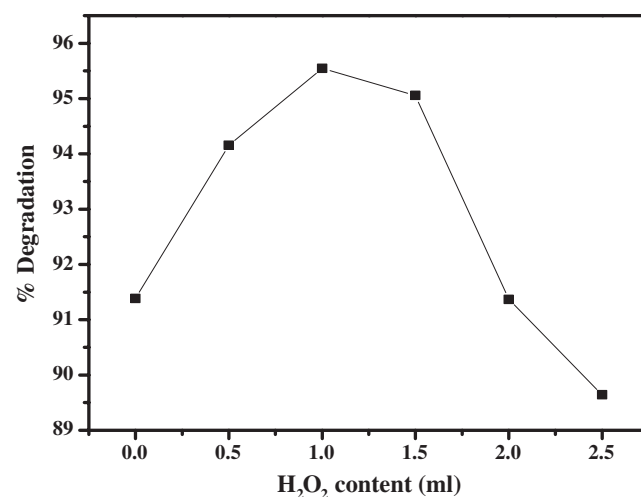


Figure 9. Effect of varying H_2O_2 content on percent degradation of indigo carmine by Ni-doped ZnS/0.5 M ZnO at room temperature and solution pH.

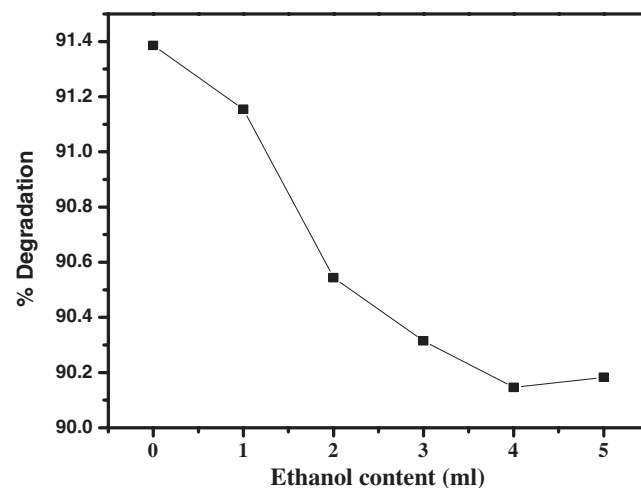


Figure 10. Effect of varying ethanol content on percent degradation of indigo carmine by Ni-doped ZnS/0.5 M ZnO at room temperature and solution pH.

3.5d *Effect of ethanol content:* The fact that hydroxyl radicals (OH^\bullet) play a major role in photodegradation processes can be ascertained through the use of alcohols such as ethanol, as alcohols are known to quench hydroxyl radical [32,33]. In this experiment, ethanol content ranging from 0 to 5 ml was added to the indigo carmine dye solution to observe its effect on the degradation efficiency of the dye. The result is given in figure 10. Degradation efficiency of the dye decreased consistently with an increase in ethanol content until at higher volumes when the efficiency begins to appreciate. The decrease in degradation efficiency can be assigned to the ability of the ethanol to quench the hydroxide radicals. However, the slight increase in degradation efficiency can be due to the formation of ethoxy radicals ($\text{C}_2\text{H}_5\text{O}^\bullet$) from direct photocatalytic oxidation of ethanol [34].

4. Conclusion

The synthesis of Ni-doped Zn/ZnO nanocomposite through chemical precipitation method has been achieved and confirmed by the various characterization techniques. XRD analysis showed the cubic and wurtzite crystalline phases of ZnS and ZnO in the Ni-ZnS/ZnO nanocomposite. Optical studies proved that modification of ZnS with Ni and ZnO caused reduction in its bandgap with corresponding improvement in its visible light activity. Photocatalytic degradation studies on the basis of catalyst doping revealed Ni-ZnS/(0.5 M ZnO) as the best photocatalyst with about 91% degradation efficiency of the dye in a pseudo-first-order kinetic manner. Photocatalytic degradation efficiency of dye was observed to increase with an increase in temperature. The degradation efficiency increased with increased H_2O_2 content up to 1 ml and decreased afterwards, while increase in ethanol content decreased the efficiency. The Ni-doped Zn/ZnO nanocomposite is regarded as an appropriate photocatalyst for degradation of indigo carmine dye in its aqueous solution.

Acknowledgements

We wish to express our gratitude to the Faculty of Science, University of Johannesburg, and Department of Applied Chemistry-Centre for Nanomaterials Science Research, National Research Foundation (TTK14052167682) and Water Research Commission of South Africa, for providing financial support to carry out this work.

References

- [1] Hoffmann M R, Martin S T, Choi W and Bahnemann D W 1995 *Chem. Rev.* **95** 69
- [2] Suzuki M, Ito T and Taga Y 2001 *Appl. Phys. Lett.* **78** 3968
- [3] Pouretdal H R, Eskandari H, Keshavarz M H and Semnan A 2009 *Acta Chim. Slov.* **56** 353
- [4] Pouretdal H R, Norozi A, Keshavarz M H and Semnani A 2009 *J. Hazard. Mater.* **162** 674
- [5] Alivisatos A P 1996 *Sci.* **271** 933
- [6] Wang Z Q, Liu Z, Gong J F, Wang S and Yang S G 2011 *Cryst. Eng. Comm.* **13** 6774
- [7] Ma H, Han J, Fu Y, Song Y, Yu C and Dong X 2011 *Appl. Catal. B: Environ.* **102** 417
- [8] Fox M A and Dulay M T 1993 *Chem. Rev.* **93** 341
- [9] Litter M I 1999 *Appl. Catal. B: Environ.* **23** 89
- [10] Bashouti M, Salalha W, Brumer M, Zussman E and Lifshitz E 2006 *Chem. Phys. Chem.* **7** 102
- [11] Marci G, Augugliaro V, Lopez-Munoz M J, Martin C, Palmisano L, Rives V and Venezia A M 2001 *J. Phys. Chem. B* **105** 1033
- [12] Fang X, Bando Y, Gautam U K, Zhai T, Zeng H, Xu X and Golberg D 2009 *Crit. Rev. Solid State Mater. Sci.* **34** 190
- [13] Lai C H, Lu M Y and Chen L J 2012 *J. Mater. Chem.* **22** 19
- [14] Chen M, Hu L, Xu J, Liao M, Wu L and Fang X 2011 *Small* **7** 2449
- [15] Huang C M, Chen L C, Pan G T, Yang T C, Chang W S and Cheng K W 2009 *Mater. Chem. Phys.* **117** 156
- [16] Navaneethan M, Archana J, Nisha K D, Hayakawa Y, Ponnusamy S and Muthamizhchelvan C 2010 *J. Alloy Compd.* **506** 249
- [17] Singh A K 2010 *Adv. Power Technol.* **21** 609
- [18] Devi B R, Raveendran R and Vaidyan A V 2007 *Pramana J. Phys.* **68** 679
- [19] Stauro B 2004 *Infrared spectroscopy: fundamentals and applications* (New York: Wiley) p 45
- [20] Brus L E 1984 *J. Chem. Phys.* **80** 4403
- [21] Kuznetsov V N and Serpone N 2006 *J. Phys. Chem. B* **110** 25203
- [22] Carp O, Huisman C L and Reller A 2004 *Prog. Solid State Chem.* **32** 33
- [23] Zhang Y, Tang Z R, Fu X and Xu Y J 2011 *ACS Nano* **5** 7426
- [24] Yu X L, Song J G, Fu Y S, Xie Y, Song X, Sun J and Du X W 2010 *J. Phys. Chem. C* **114** 2380
- [25] Sakthivel S and Kisch H 2003 *Angew. Chem. Int. Ed.* **42** 4908
- [26] Serpone N, Lawless D and Khairutdinov R 1995 *J. Phys. Chem.* **99** 16646
- [27] Sunitha S, Rao A N and Karthikeyan J 2015 *Orient. J. Chem.* **31** 107
- [28] Bose S, Galande C, Chockalingam S P, Banerjee R, Raychaudhuri P and Ayyub P 2009 *J. Phys.-Condens. Mat.* **21** 205702
- [29] Prado A G, Bolzon L B, Pedroso C P, Moura A O and Costa L L 2008 *Appl. Catal. B: Environ.* **82** 219
- [30] Aguedach A, Brosillon S, Morvan J and Lhadi E K 2005 *Appl. Catal. B: Environ.* **57** 55
- [31] Zhu C, Wang L, Kong L, Yang X, Wang L, Zheng S and Zong H 2000 *Chemosphere* **41** 303
- [32] Qourzal S, Tamimi M, Assabbane A and Ait-ichou Y 2007 *C.R. Chim.* **10** 1187
- [33] Saien J, Delavari H and Salman A R 2010 *J. Hazard. Mater.* **177** 1031
- [34] Alahiane S, Qourzal S, Ouardi M E, Abamrane A and Assabbane A 2014 *Am. J. Anal. Chem.* **5** 445